Simulation of thermoplastic prepreg thermoforming based on a visco-hyperelastic model and a thermal homogenization

Eduardo Guzman Maldonado, Nahiène Hamila, Naïm Naouar, G. Moulin, Philippe Boissé

Simulation of thermoplastic prepreg thermoforming based on a visco-hyperelastic model and a thermal homogenization

E. Guzman-Maldonado, N. Hamila, N. Naouar, G. Moulin, P. Boisse

PII: S0264-1275(15)31024-8
DOI: doi: 10.1016/j.matdes.2015.12.166
Reference: JMADE 1190

To appear in:

Received date: 31 October 2015
Revised date: 28 December 2015
Accepted date: 29 December 2015

Please cite this article as: E. Guzman-Maldonado, N. Hamila, N. Naouar, G. Moulin, P. Boisse, Simulation of thermoplastic prepreg thermoforming based on a visco-hyperelastic model and a thermal homogenization, (2015), doi: 10.1016/j.matdes.2015.12.166

Simulation of thermoplastic prepreg thermoforming based on a visco-hyperelastic model and a thermal homogenization

E. Guzman-Maldonado[1], N. Hamila[1], N. Naouar[1], G. Moulin[2], P. Boisse[1*]

[1] Université de Lyon, LaMCoS UMR 5259, INSA-Lyon, 27 Av. Jean Capelle, F-69621, Villeurbanne, France

[2]PLASTIC OMNIUM Recherche & développement. Av. du Bois des Vergnes F-01150 Ste Julie, France

Abstract

The simulation of thermoplastic prepreg forming is achieved by alternating thermal and forming analyses. The thermal properties are obtained from a mesoscopic analysis and a homogenization procedure. The forming simulation is based on a viscous-hyperelastic approach. The thermal simulations define the coefficients of the mechanical model that depends on the temperature. The forming simulations modify the boundary conditions and the internal geometry of the thermal analyses. The comparison of the simulation with an experimental thermoforming of a part representative of automotive applications shows the efficiency of the approach.

Keywords

Prepreg, Thermoplastic resin, Forming, Thermomechanical, Viscoelasticity, Finite Element Analysis.

Introduction

Composite materials made of continuous fibers (carbon, glass, aramid, etc.) and polymer matrix are used for their good mechanical properties associated with a low density. The recent commercial and military aircraft make great use of composite materials in their airframes and primary structures. There is also an active interest in this type of materials in the automotive industry to reduce the mass of the components and consequently the fuel consumption of vehicles [1, 2]. Nevertheless, the high production rates of these industries require rapid manufacturing processes (typically one to five minutes).

Thermoforming thermoplastic prepreg with continuous fiber is a fast process that can be used for car structures manufacturing [3,4]. The process takes a few minutes, and the continuous reinforcements give good material properties. The thermoforming stage of the process example that is analyzed in this paper takes twenty seconds. In addition, composite materials with thermoplastic matrix are more easily recyclable than those using thermoset resins. This topic is important for the automotive industry.

Several parameters affect a thermoforming process of CFRTP (continuous fiber reinforced thermoplastic) composites [5]: temperature, loads on the tools, blank holders, orientation of the plie, etc. Manufacturing double curved parts without defects (wrinkling, porosities, fiber fracture, etc.) can be difficult. In order to avoid “trial and error” processes, simulation codes for composite manufacturing have been developed to determine and optimize the manufacturing conditions [5-10].

* Corresponding author: P.Boisse, INSA Lyon, France, philippe.boisse@insa-lyon.fr; tel. +33 4 72 43 63 96

This article presents an approach for the simulation of thermoplastic prepreg thermoforming. The simulation is based on a viscoelastic behavior with a strong thermal dependency. The forming is performed at a temperature slightly higher than the melting point of the resin. Consequently, a small variation of this temperature strongly modifies the mechanical behavior of the prepreg during forming. The simulation is made within a finite element approach. Each ply is modeled as a continuous shell. Continuous models have been proposed for fiber reinforced materials by Spencer [11,12]. These models are based on the fiber inextensibility. They have been extended, in particular, to viscoelastic behavior [13-20].

Given the growing interest in thermoplastic prepreg thermoforming, some commercial codes have been developed for the simulation of these processes. In particular, the Pam-Form™ code [5] based on an explicit F.E.M approach and the AniForm™ code [18] based on an implicit approach.

Recent papers analyze the thermoforming processes of thermoplastic prepregs. In [21] the influence of the different process parameters was experimentally evaluated. The process simulation presented in [22] is based on a non-orthogonal constitutive model originally developed by Yu et al. [23] and implemented in a user subroutine of code Abaqus Explicit™. The simulations of a double dome geometry thermoforming were compared to the experiments, but wrinkles are not simulated since membrane and truss elements are used. In [18], simulations using AniForm™ software are compared to the experiments in cases of thermostamping unidirectional and woven textile reinforced prepregs. In both works [22] and [18], the mechanical properties of the prepreg depend on the temperature, but this is assumed to be constant in the blank. However, as it will be shown below, the temperature distribution evolves during forming phase due to the contacts with the tools. The current work aims to present both modeling of the thermal phenomena including the evolution of temperature fields and the simulation of the blank deformation using a finite strain viscoelastic model. The coupling between the thermal and mechanical problems is obtained by performing alternatively both simulations. The thermal properties are obtained from a homogenization procedure taking in count the deformation of the unit cell as a result of the forming. The viscoelastic model is an extension of the work of Simo [24] to the case of thermoplastic prepreg shells with a viscous behavior in in-plane shear.

The thermoforming of an industrial part is carried out both by experimental methods and by numerical simulations based on the presented approach. The comparison between experiments and simulations shows good results.

2- Thermoforming of thermoplastic prepregs

2.1. Stages of the process

The thermoplastic composite thermoforming process consists of four principal stages (Fig. 1). First, the thermoplastic plate is heated by infra-red to a temperature slightly higher than the melting point of the matrix. A robotic arm transports the heated prepreg blank to a mold that is heated to a lower temperature than the blank. This temperature is chosen to ensure a good surface quality and a short cycle time.

The mold closes and shapes the composite part. A pressure is then applied in order to crystallize and consolidate the composite. This step must ensure that there are few porosities in the composite part.

2.2. Material

The base material considered in the present study is an 8-Harness Satin PA66/Glass thermoplastic pre-preg. The material is presented as a pre-consolidated blank made out of 5 plies with a [0/90] stacking sequence. The main characteristics of the composite are given in table A.1 in Annexe A. Its melting temperature is between 257°C and 265°C, and the solidification temperature is between 217°C and 225°C. This temperature depends on the heating and cooling rates (Fig. 2). After the heating step, the temperature blank is at a uniform temperature of 300°C and decrease by 3°C per second by convection. The contact of the blank with the tools leads to a thermal shock that renders a non-uniform temperature distribution in the prepreg.

2.3. Manufactured part

The manufactured part which is analyzed in this work is showed in Fig. 3. It is representative of composite parts for automotive applications. The shape is strongly double curved at the end of the part. The forming needs large shear angles and wrinkles can appear. These wrinkles disrupt the consolidation stage. It is necessary to check that they do not reach the useful part of the composite.

2.4. Objective of the process simulation

The thermoforming simulations aim to determine the feasibility of the process and its conditions [21]. The in-plane shear angles, the possible wrinkles and the compaction/consolidation state are the principal quantities that characterize the thermoforming process, and that will be calculated by the simulation. Because the mechanical behavior is strongly temperature-dependent, thermal analysis and forming simulations are performed alternately. The thermal analysis gives updated parameters of the mechanical behavior. The forming simulation updates the geometry and the tool blank contact zone of the analysis.

The mechanical and thermal material properties must be known. In-plane shear properties are analyzed by a bias-extension test at high temperature [25-27]. Bending properties are determined using a cantilever bending test at temperature [28]. The thermal properties depend on the deformation, on the temperature and on the cooling rate. They are difficult to measure. In this paper, they are determined by a mesoscopic analysis (section 3). A visco-hyperelastic model is presented in section 4, the coefficients of this law are all thermo-dependent and updated by the thermal analyses.

3- Thermal analyses

During the forming simulation, the temperature field is calculated in order to update mechanical parameters that are strongly thermo-dependent. In order to compute this temperature field, the thermal properties of the composite at the macroscale must be known.

The heat capacity of the fiber/polymer mix can be evaluated using a rule of mixture. Another way consists of measuring it using DSC like the one presented in Fig. 2. This popular thermal analysis uses the temperature difference developed between a sample and a reference for the calculation of the heat flow. This allows to determine the material's heat capacity and the enthalpies of transition as a function of temperature and the heating/cooling rate. These both methodologies have flaws and qualities. The weakness of the first approach is related to the presence of fibers inside a polymer that leads to higher crystallization phenomena. This results in a higher phase change enthalpy [29]. DSC measurement may seem to be an alternative to measure directly the fiber / matrix heat capacity. However, the sample size is small and having samples with the same fiber ratio is a hard challenge. This is the reason why the evaluation of the heat capacity using the rule of mixtures was adopted as the first approach.

The thermal conductivities are determined by mesoscopic analysis. The woven reinforced prepreg has a periodicity that can be exploited to perform a homogenization simulation and get the macroscopic conductivity from the geometry of the mesostructure from the thermal properties of the yarns and the polymer.

3.1 Homogenization method

The periodicity of material properties and geometry of the structure can be used to perform homogenization using specific boundary conditions. In this work, the equivalent conductivity tensor is calculated using the homogenization technique proposed by [30] on a single RVE (Representative Volume Element).

The starting point is the use of the thermal gradient at the macroscopic scale (assumed known) to impose the boundary conditions at the mesoscopic scale. The macroscopic conductivity tensor is then estimated by averaging the resulting mesoscopic flux at the boundary conditions. Theoretically, this method doesn't apply any constraint to the RVE material's components (anisotropy, temperature dependence, etc.). It can take into account the geometric evolution of the structure after deformation. Without sources of energy, internal thermal equilibrium is given by:

$$\underline{\nabla}_m \cdot \underline{q}_m(\underline{x}) = 0 \tag{1}$$

Where $\underline{q}_m$ represents the volumetric heat flow at the point $\underline{x}$ of the mesoscopic structure. Let's consider the volume Ω_m containing the sheared RVE bounded by the faces A, B, C, D, E, F presented Fig. 4. Given the temperature at the macroscopic scale T_M and at the mesoscopic scale T_m, the macroscopic temperature gradient $\underline{\nabla}_M T_M$ and mesoscopic averaged gradient $\underline{\nabla}_m T_m$ verify the equality:

$$\frac{1}{V}\int_{\Omega_m} \underline{\nabla}_m T_m dV = \underline{\nabla}_M T_M \tag{2}$$

It is obtained by imposing at the edge of the mesoscopic structure the following conditions:

$$\begin{aligned} T_{m_B} - T_{m_A} &= \underline{\nabla}_M T_M \cdot \left(\underline{x}_B - \underline{x}_A\right) \\ T_{m_D} - T_{m_C} &= \underline{\nabla}_M T_M \cdot \left(\underline{x}_D - \underline{x}_C\right) \\ T_{m_F} - T_{m_E} &= \underline{\nabla}_M T_M \cdot \left(\underline{x}_F - \underline{x}_E\right) \end{aligned} \tag{3}$$

where T_{m_i} corresponds to the mesoscopic temperature at point $\underline{x}_i$. The point $\underline{x}_B$ on side B, corresponds to the point $\underline{x}_A$ of side A by simple periodic translation, and similarly for $\underline{x}_D$ with $\underline{x}_C$ or $\underline{x}_F$ with $\underline{x}_E$. These conditions are known from the periodic boundary conditions and naturally lead to antiperiodic boundary conditions in terms of heat flows through the domain:

$$\begin{aligned} \underline{q}_{m_B} \cdot \underline{n}_1 &= -\underline{q}_{m_A} \cdot \underline{n}_1 \\ \underline{q}_{m_D} \cdot \underline{n}_2 &= -\underline{q}_{m_C} \cdot \underline{n}_2 \\ \underline{q}_{m_F} \cdot \underline{n}_3 &= -\underline{q}_{m_E} \cdot \underline{n}_3 \end{aligned} \tag{4}$$

$\underline{n}_1$, $\underline{n}_2$ and $\underline{n}_3$ being the normal vectors to the faces B, D and F at the points $\underline{x}_B$, $\underline{x}_D$ and $\underline{x}_F$. The computation of the macroscopic flux from the mesoscopic flux is done by taking the average of the flow at mesoscopic scale:

$$\frac{1}{V}\int_{\Omega_m} \underline{q}_m dV = \underline{q}_M \tag{5}$$

It has been shown in [30] that taking the average in this form ensures the consistency of entropy between the macroscopic and mesoscopic scale:

$$\frac{1}{V}\int_{\Omega_m} \underline{\nabla}_m T_m . \underline{q}_m dV = \underline{q}_M . \underline{\nabla}_M T_M \tag{6}$$

Once the macroscopic flow $\underline{q}_M$ is calculated, it is connected to the macroscopic temperature gradient $\underline{\nabla}_M T_M$ by the macroscopic conductivity $\underline{\underline{K}}_M$:

$$\underline{q}_M = \underline{\underline{K}}_M \underline{\nabla}_M T_M \tag{7}$$

In matrix form:

$$\begin{Bmatrix} \underline{q}_{M_1} \\ \underline{q}_{M_2} \\ \underline{q}_{M_3} \end{Bmatrix} = \begin{bmatrix} k_{11} & k_{12} & k_{13} \\ k_{21} & k_{22} & k_{23} \\ k_{31} & k_{32} & k_{33} \end{bmatrix} \begin{Bmatrix} \left(\underline{\nabla}_M T_M\right)_1 \\ \left(\underline{\nabla}_M T_M\right)_2 \\ \left(\underline{\nabla}_M T_M\right)_3 \end{Bmatrix} \tag{8}$$

Each column of $\underline{\underline{K}}_M$ is calculated imposing three different periodic boundary conditions:

$$\underline{\nabla}_M T_M = \begin{bmatrix} 1 & 0 & 0 \end{bmatrix}^T, \quad \underline{\nabla}_M T_M = \begin{bmatrix} 0 & 1 & 0 \end{bmatrix}^T, \quad \underline{\nabla}_M T_M = \begin{bmatrix} 0 & 0 & 1 \end{bmatrix}^T \tag{9}$$

3.2 Application to the analyzed thermoplastic prepreg

The non-deformed mesoscopic structure was determined using X-ray micro-computed tomography (µCT) (Fig. 5a) [31, 32]. Then the geometric is modelled using the TexGen software developed at the University of Nottingham as a modelling pre-processor for textiles [33]. The local direction of the fibers is provided by TexGen and is later used to manage the anisotropy of the meshes (Fig. 5). The cho-

sen homogenization method implies that the thermal properties of the constituents at the mesoscopic scale (fiber yarns and matrix) are known. Outside the yarns, it is assumed that the behavior of the polymer is isotropic but depends on the temperature. The thermal conductivity of PA 6.6 (k_p), is given Fig. 6 [34]. The conductivity of glass fibers (k_f) will be assumed to be constant and equal to $1\,\mathrm{Wm^{-1}K^{-1}}$ [35]. It is assumed that the conductivity inside the yarn is transversely isotropic, i.e. the conductivity in the longitudinal direction (parallel to the fiber direction) and transverse (perpendicular to the fiber direction) are different. The longitudinal and transverse conductivities can be deducted from the analytical relations derived from Maxwell and Rayleigh's theory. Locally, a yarn can be modeled as a series of cylindrical inclusions (fibers) embedded in an isotropic medium (the matrix). In this configuration, the thermal conductivity k_{lon}^{y} in the longitudinal direction can be approximated by a simple rule of mixture of the form:

$$k_{lon}^{y} = k_f \cdot v_f^{y} + k_p \cdot \left(1 - v_f^{y}\right) \tag{10}$$

where v_f^{y} represents the volume fraction of the fibers inside the yarn deduced from the image processing of the µCT [31], k_f and k_p are the conductivity of fibers and polymer. As regards the transverse conductivity k_{tra}^{y}, [36] proposes an analytical formula which takes into account the conductance between the fiber and the matrix:

$$k_{tra}^{y} = k_p \cdot \frac{\left(\frac{k_f}{k_p} - 1 - \frac{k_f}{a h_c}\right) v_f^{y} + \left(1 + \frac{k_f}{a h_c} + \frac{k_f}{k_p}\right)}{\left(1 + \frac{k_f}{a h_c} - \frac{k_f}{k_p}\right) v_f^{y} + \left(1 + \frac{k_f}{a h_c} + \frac{k_f}{k_p}\right)} \tag{11}$$

h_c being the conductance at to the fiber-matrix interface and a the radius of the fiber. In this work, full contact is considered, giving $h_c \to \infty$:

$$k_{tra}^{y} = k_p \cdot \frac{\left(\frac{k_f}{k_p} - 1\right) v_f^{y} + \left(1 + \frac{k_f}{k_p}\right)}{\left(1 - \frac{k_f}{k_p}\right) v_f^{y} + \left(1 + \frac{k_f}{k_p}\right)} \tag{12}$$

A voxelized model is considered in order to facilitate the implementation of all periodic boundary conditions. The finite element meshes on the different sides of the domain are by default considered coincident independently of the mesostructure and the node to node relation can be established. The boundary conditions are introduced between corresponding nodes using the macroscopic temperature gradient. The macroscopic temperature gradients applied in equation 9 are represented Fig.7.

A set of simulations was performed for different in-plane shear angles and at different temperatures to express the macro scale conductivity as a function of shear angle (γ) and a function of the temperature

in the orthonormal basis $(\underline{e}_1, \underline{e}_2, \underline{e}_3)$, where $\underline{e}_1$ is collinear to the fiber. The components of the conductivity tensor are plotted in the Fig. 8. They are later used during the forming simulation to compute the temperature field on the composite at the macro scale and determine the mechanical properties of the prepreg as depicted in section 4.

4. Visco-hyperelastic model

4.1 In plan shear viscoelasticity

During a prepreg thermoforming process, the in-plane shear deformation plays a main role. Given the quasi-inextensibility of the fibres, draping on a double curved shape is made possible through significant in-plane shear deformations. Consequently, a non-linear visco-elastic model in in-plane shear is considered in the present paper. The tensile behavior in fibre direction is very stiff and mainly depends on the fibre tensile behavior that is not viscous. It has been shown that the bending stiffness influences the forming of thermoplastic prepreg, in particular, wrinkles [28, 37]. But this influence manifests itself slowly with regards to bending stiffness variation. In addition, there are few references on prepreg bending properties and even less on viscous bending properties. It is assumed in the present work that viscosity only affects the in-plane shear behavior. This is consistent with the approach proposed by Simo [24] and Holzapfel [38] that only consider the viscosity in the deviatoric part of the behavior. Fig. 9 shows the load versus time in an in-plane shear test. This experiment is a bias-extension test performed at 270°C increasing the displacement of the clamp per stage. The relaxation effects are large confirming the viscoelastic shear behavior.

4.2. Constitutive model

The visco-hyperelastic model used for in-plane shear behavior can be seen as an extension of the generalized relaxation model. This one is made of a free spring arranged in parallel with n Maxwell elements (Fig. 10). The stiffnesses of the free spring and for the spring of the Maxwell element number i are determined by the Young's moduli E_∞ and E_i, i=1,…,n. The viscous behavior is described by the dashpots with a constant viscosity η_i.

The existence of a free energy function ψ is assumed [24]. Denoting $\underline{\underline{C}}$ the right Cauchy-Green strain tensor and Q_i a set of internal variables:

$$\begin{aligned}\psi(\underline{\underline{C}},\underline{\underline{Q}}_i) = {} & w^1_{elong}(I^1_{elong}) + w^2_{elong}(I^2_{elong}) + w^1_{bend}(I^1_{bend}) + w^2_{bend}(I^2_{bend}) + w_{shear}(I_{shear}) \\ & -\frac{1}{2}\sum_{i=1}^{N}\left(\underline{\underline{C}} : \underline{\underline{Q}}_i\right) + \Xi\left(\sum_{i=1}^{N}\underline{\underline{Q}}_i\right)\end{aligned} \tag{13}$$

The parameters $I^1_{elong}, I^2_{elong}, I^1_{bend}, I^2_{bend}, I_{shear}$ are invariants in tension, bending and in-plane shear. $w^1_{elong}, w^2_{elong}, w^1_{bend}, w^2_{bend}, w_{shear}$ are the corresponding potential energies that are assumed to be uncoupled.

The invariants used in the case of a material with yarns in warp and weft directions have been given in function of $\underline{\underline{C}}$ in [39, 40]:

$$I^1_{elong} = \frac{1}{2}\ln\left(\underline{\underline{C}} : \underline{L}_1 \otimes \underline{L}_1\right) \qquad I^2_{elong} = \frac{1}{2}\ln\left(\underline{\underline{C}} : \underline{L}_2 \otimes \underline{L}_2\right) \tag{14}$$

$$I_{shear} = \frac{\left(\underline{\underline{C}} : \underline{L}_1 \otimes \underline{L}_2\right)}{\sqrt{\left(\underline{\underline{C}} : \underline{L}_1 \otimes \underline{L}_1\right)\left(\underline{\underline{C}} : \underline{L}_2 \otimes \underline{L}_2\right)}} = \sin(\gamma) \tag{15}$$

$$I^1_{bending} = \underline{l}_1 \cdot \underline{\underline{\chi}} \cdot \underline{l}_1 = \chi_{11} \qquad I^2_{bending} = \underline{l}_2 \cdot \underline{\underline{\chi}} \cdot \underline{l}_2 = \chi_{22} \tag{16}$$

where $\underline{\underline{\chi}}$ denotes the curvature tensor, $\underline{L}_1, \underline{L}_2$ are the unit vector in the initial warp and weft directions and $\underline{l}_1, \underline{l}_2$ the unit vector in the current warp and weft directions.

The stress resultants are derived from the free energy function.

Tension resultant:

$$\underline{\underline{N}}_{elong} = 2\left(\frac{\partial w^1_{elong}}{\partial I^1_{elong}}\frac{\partial I^1_{elong}}{\partial \underline{\underline{C}}} + \frac{\partial w^2_{elong}}{\partial I^2_{elong}}\frac{\partial I^2_{elong}}{\partial \underline{\underline{C}}}\right) \tag{17}$$

In-plane shear resultant:

$$\underline{\underline{N}}_{shear} = 2\frac{\partial w_{shear}}{\partial I_{shear}}\frac{\partial I_{shear}}{\partial \underline{\underline{C}}} - \sum_{i=1}^{N}\underline{\underline{Q}}_i \tag{18}$$

Bending moments

$$M_{11} = \frac{1}{J}\frac{\partial w_{bend}}{\partial I^1_{bend}} \qquad M_{22} = \frac{1}{J}\frac{\partial w_{bend}}{\partial I^2_{bend}} \tag{19}$$

J being the r ratio between the current and initial surface. The viscoelastic internal variables are solution of the following equations [24]:

$$\begin{cases} \dot{\underline{\underline{Q}}}_i(t) + \dfrac{1}{\tau_i}\underline{\underline{Q}}_i(t) = \dfrac{\gamma_i}{\tau_i}\left[2\dfrac{\partial w_{shear}}{\partial I_{shear}}\dfrac{\partial I_{shear}}{\partial \underline{\underline{C}}}\right] \\ \lim\limits_{t\to-\infty}\underline{\underline{Q}}_i(t) = 0 \end{cases} \tag{20}$$

γ_i are dimensionless material's parameter such as $0 < \gamma_i < 1$, $\gamma_\infty = 1 - \sum_{i=1}^{N}\gamma_i$ and $0 \le \gamma_\infty < 1$.

τ_i are the relaxation times. The solution of equation (20) can be expressed as a convolution integral:

$$\underline{\underline{Q}}_i(t) = \frac{\gamma_i}{\tau_i}\int_{-\infty}^{t}\exp\left(\frac{s-t}{\tau_i}\right)\frac{\mathrm{d}}{\mathrm{d}s}\left[2\frac{\partial w_{shear}}{\partial I_{shear}}\frac{\partial I_{shear}}{\partial \underline{\underline{C}}}\right]\mathrm{d}s \tag{21}$$

Consequently, the in-plane shear resultant is:

$$\underline{\underline{N}}_{shear}(t) = \int_{-\infty}^{t}\left(\gamma_\infty + \sum_{i=1}^{N}\gamma_i\exp\left(\frac{s-t}{\tau_i}\right)\right)\frac{\mathrm{d}}{\mathrm{d}s}\left[2\frac{\partial w_{shear}}{\partial I_{shear}}\frac{\partial I_{shear}}{\partial \underline{\underline{C}}}\right]\mathrm{d}s \tag{22}$$

All the parameters of the present model depend on the temperature. They are assumed to be piecewise linearly dependent on the temperature in the interval of study [260°C- 300°C].

4.3. Material parameter identification

4.3.1 In-plane shear properties

The in-plane shear mechanical behavior is identified using a bias-extension test [25-27, 41-44]. The picture frame experiment is a possible alternative [22, 45, 46]. The following in-plane shear energy potential is considered:

$$w_{shear} = \sum_{k=1}^{3} C_k \left(I_{shear} \right)^{2k} \tag{23}$$

A Levenberg–Marquardt algorithm is used to identify the material parameters γ_i, the relaxation times τ_i and the coefficients C_k from a bias-extension test with loading steps (Fig. 11). The identification is made for four temperatures between 260°C and 300°C. The parameters of intermediate temperatures are linearly interpolated. The identified viscoelastic properties are given in table A.2 and A.3 in annexe A.

4.3.2 Bending properties

The identification of bending properties is made using a cantilever test performed in an environmental chamber [28, 47-49] (Fig. 12). The specimen is clamped at one edge and loaded by its own weight. The deflections at different temperatures are measured by a CCD camera.

The curvature of these curves is computed and bending moment versus curvature curves can be plotted for different temperatures (Fig. 12c). The bending stiffness is strongly depending on the temperature. The bending potential energy is in the form:

$$w^1_{bend} = B_1 \left(I^1_{bend} \right)^2 \qquad w^2_{bend} = B_2 \left(I^2_{bend} \right)^2 \tag{24}$$

The identified viscoelastic properties are given in table A.4 in annexe A. The dynamic Mechanical Analysis (DMA) system can be an option for the out-of-plane bending properties [50].

4.3.3 Tensile properties

The tensile properties should be determined from tensile tests at different temperatures. The tensile behavior is biaxial [51, 52]. Nevertheless, the tensile rigidities are large and play the role of inextensibility constraints in forming simulations. In this study, the tensile rigidities T_1 and T_2 are assumed to be constant and independent of the temperature.

$$w^1_{elong} = T_1 (I^1_{elong})^2 \qquad w^2_{elong} = T_2 (I^2_{elong})^2 \tag{25}$$

For simplicity, the tensile stiffness of the prepreg is calculated from the young modulus of the fibers (glass), the number of fibers and their section. This number of fibers is set by the fiber volume fraction and the thickness of the prepreg. Table A.5 gives the tensile stiffnesses in Annexe A.

4.3.4 Speed Effects

The visco-elastic model described above depends on the loading rate. In the case of a bias-extension test, Fig. 13 shows the comparison between the experimentally measured load and the computed load using the visco-hyperelastic model. The bias-extension test is performed at 30 mm/min and 150 mm/min. The loading curves at these two speeds are significantly different. This difference is well depicted by the simulation base on the presented model.

5. Numerical simulations and comparison with experimental process

The constitutive model described above has been implemented in the finite element code Plasfib [53] based on an explicit dynamic approach. The blank is discretized by triangular shell elements without rotational degrees of freedom. The curvatures of the element are computed from the position of the neighbor elements [54-56]. The coupling between the thermal and mechanical problem is obtained by performing alternately forming simulations (that modify both the boundary of the thermal problem and the values of the thermal conductivity as described in section 3) and thermal computations (that modify the mechanical properties).

The simulation of the composite part thermoforming presented in section 2.3 is performed. The processing time is 19 s (for the forming stage). The thermal conductivity is obtained from the homogenization procedure presented in section 3. The update of the temperature distribution in the material has been considered since the contact surfaces increase during forming. It is assumed that the contact conductance between the tools and the prepreg is constant and equal to 1000 [$Wm^{-2}K^{-1}$] although this property depends on the contact pressure, the temperature and the physical and geometrical properties of the materials [57].

The geometry of the analyzed part is rather complex. It is double curved, and some wrinkles appear during the thermoforming process. The simulation has to determine the conditions for which these wrinkles do not spread to the useful part of the composite. The numerical model is presented in Fig. 14 and is composed of a punch, a die and a rectangular blank (750x800 mm). The processing conditions have been imposed as follows: the initial temperature of the blank was fixed to 300°C. It was assumed that the temperature of the tools remains constant and equal to 250°C. The forming process has been carried out with a constant punch velocity of 240 mm/min. As mentioned above, the coupling between the thermal and mechanical problems is obtained by alternating thermal and mechanical simulation. The local orientation of the yarns resulting from the mechanical is considered to define a local coordi-

nate system according to the orthonormal basis defined in section 3.2. The local conductivity tensor can be inferred in this basis from the local shear angle and the local temperature. The mechanical properties depend on the temperature field calculated by these analyses. Fig. 15. shows the temperature computed in the blank at different times of the thermoforming process.

The deformed shapes at different forming stages are compared to the experimental process in Fig**Error! Reference source not found.** 16. In order to obtain experimental intermediate deformed shapes, the process has been stopped at given punch displacements by placing different chocks between the tools. The agreement between the process simulations and the experiments is rather good. Some wrinkles occur in the experimental parts. They are fairly well described by the simulations. Because the shape is strongly double curved, the forming needs large in-plane shear in the blank. These shear angles are important results of the simulation. First, they define the orientation of the fibers in the composite part that mainly influence its mechanical properties. Secondly, the risk of wrinkling in a shaping process increases much for large shear angles [37, 49, 58].

A recess is present in the central portion of the composite part (indicated as zone A in Fig. 16f). In the first stage of the forming, this recess is a bump to the top. Fig. 17 shows the evolution of this bump as a function of the punch displacement (d) in comparison with the experimental profile. The presence of the bump is well obtained by the simulation, although the computed shape of the bump is somewhat smaller than the experimental one. At the end of the punch travel, both experimental and simulated displacements are reduced to zero before taking on the shape of the recess.

6. Conclusions

A simulation approach of thermoplastic prepreg thermoforming has been presented and has shown its predictive capability. The computed shear angles were shown to match the experimental results correctly. The wrinkle developments are also reasonably well simulated. The simulation is composed of thermal analyses and forming simulations performed alternatively. This ensures a coupling between the mechanical and thermal simulations. The deformation of a unit cell and the modification of contacts with the tools change the local thermal properties and temperatures. It has been shown that the temperature field is significantly modified during the forming. This is important because the mechanical behavior of prepreg strongly depends on temperature. In conclusion, the proposed coupled thermomechanical approach has confirmed that this coupling is necessary for the thermoforming of thermoplastic prepregs, and that the assumption of constant temperature in the blank is not sufficient in the case of the thermoforming of an automotive part.

The next development which is underway will be the analysis of compaction/consolidation [59-61]. It is important to ensure the removal of porosities in the compaction stage. The quality of the composite part mainly depends on this point. The simulation must predict the compaction and consolidation of the

composite. The through the thickness analysis require both finite elements with transverse deformation [62, 63] and compaction and consolidation laws [59, 60, 64, 65].

Acknowledgements

The work was made within the framework of the FUI project Composite Cab. The authors wish to thank the Rhône-Alpes region for funding this work. The authors also thank collaborations with Plastic Omnium, Solvay and Volvo.

Appendix A. Material data used in the forming simulations

Matrix	**PA66**
Fibres	E-Glass
Fabric wave	8-Harness Satin
Fibre volume (%)	48
Void content (%)	< 0.2
Areal density (g.m^{-2})	546
Thickness (mm)	2

Table A.1 Main material properties

$w_{shear}(I_{shear},T)=\begin{cases}\left(\alpha_1^w T+\beta_1^w\right)\sum_{k=1}^{3}C_k\left(I_{shear}\right)^{2k}\\ \left(\alpha_2^w T+\beta_2^w\right)\sum_{k=1}^{3}C_k\left(I_{shear}\right)^{2k}\end{cases}$	$260°C \le T \le 270°C$ $270°C < T \le 300°C$
α_1^w = -6.010e-02 K^{-1} α_2^w = -6.709e-03 K^{-1}	β_1^w=1.663e+01 β_2^w=2.206e+00
C_1 = 6.122e-01 J/mm^2 C_2 = 6.794e-01 J/mm^2 C_3 = -3.756e-02 J/mm^2	

Table A.2. In-plane shear elastic properties

$\gamma_i(T)=\alpha_i^\gamma T+\beta_i^\gamma$	$\tau_i(T)=\alpha_i^\tau T+\beta_i^\tau$
α_1^γ = -1.793e-03 α_2^γ = 6.845e-04	α_1^τ = 1.706e-02 [K·s^{-1}] α_2^τ = -4.527e-02 [K·s^{-1}]
β_1^γ=1.397e+00 β_2^γ=-1.491e-01	β_1^γ = -3.715e+00 [s] β_2^γ = 4.642e+01 [s]

Table A.3. In-plane shear viscous properties

$B_1(T)=B_2(T)=b_1\,\mathrm{T}\ +\ b_2 \quad \mathrm{T}\in[260,300]$
$b_1=-0.01838\left[\mathrm{N\cdot mm\cdot K^{-1}}\right]$ $b_2=6.438\ \left[\mathrm{N\cdot mm}\right]$

Table A.4 Bending properties

$T_1=T_2=1.095e^{+04}$ Mpa

Table A5 Tensile rigidities

References

[1] Verrey, J., Wakeman, M. D., Michaud, V., & Månson, J. A. (2006). Manufacturing cost comparison of thermoplastic and thermoset RTM for an automotive floor pan. *Composites Part A: Applied Science and Manufacturing*, 37(1), 9-22.

[2] Fuchs, E. R., Field, F. R., Roth, R., & Kirchain, R. E. (2008). Strategic materials selection in the automobile body: Economic opportunities for polymer composite design. *Composites Science and Technology*, 68(9), 1989-2002.

[3] MallicK, P. K. (2010). Thermoplastics and thermoplastic–matrix composites for lightweight automotive structures. Materials, *Design and Manufacturing for Lightweight Vehicles*, 174.

[4] Friedrich, K., & Almajid, A. A. (2013). Manufacturing aspects of advanced polymer composites for automotive applications. *Applied Composite Materials*, 20(2), 107-128.

[5] De Luca, P., Lefebure, P., & Pickett, A. K. (1998). Numerical and experimental investigation of some press forming parameters of two fibre reinforced thermoplastics: APC2-AS4 and PEI-CETEX. *Composites Part A: Applied Science and Manufacturing*, 29(1), 101-110.

[6] Boisse, P. (2007). Finite element analysis of composite forming. *Composites forming technologies*, Woodhead Publishing, 46-79.

[7] Ten Thije, R. H. W., & Akkerman, R. (2009). A multi-layer triangular membrane finite element for the forming simulation of laminated composites. *Composites Part A: Applied Science and Manufacturing*, 40(6), 739-753.

[8] Allaoui, S., Boisse, P., Chatel, S., Hamila, N., Hivet, G., Soulat, D., & Vidal-Salle, E. (2011). Experimental and numerical analyses of textile reinforcement forming of a tetrahedral shape. *Composites Part A: Applied Science and Manufacturing*, 42(6), 612- 622.

[9] Gereke, T., Döbrich, O., Hübner, M., & Cherif, C. (2013). Experimental and computational composite textile reinforcement forming: A review. *Composites Part A: Applied Science and Manufacturing*, 46, 1-10.

[10] Hübner, M., Rocher, J. E., Allaoui, S., Hivet, G., Gereke, T., & Cherif, C. (2015). Simulation-based investigations on the drape behavior of 3D woven fabrics made of commingled yarns. *International Journal of Material Forming*, on line, DOI 10.1007/s12289-015-1245-8

[11] Spencer, A. J. M. (1972). Deformations of fibre-reinforced materials. London: Oxford Univ. Press.

[12] Spencer, A. J. M. (Ed.). (1984). *Continuum theory of the mechanics of fibre-reinforced composites* (Vol. 282, pp. 1-32). New York: Springer.

[13] Rogers, T. G. (1989). Rheological characterization of anisotropic materials. *Composites*, 20(1), 21-27.

[14] McGuinness, G. B., & ÓBrádaigh, C. M. (1997). Development of rheological models for forming flows and picture-frame shear testing of fabric reinforced thermoplastic sheets. *Journal of Non-Newtonian Fluid Mechanics*, 73(1), 1-28.

[15] Hsiao, S. W., & Kikuchi, N. (1999). Numerical analysis and optimal design of composite thermoforming process. *Computer methods in applied mechanics and engineering*, 177(1), 1-34.

[16] Spencer, A. J. M. (2000). Theory of fabric-reinforced viscous fluids. *Composites Part A: Applied Science and Manufacturing*, 31(12), 1311-1321.

[17] Harrison, P., Yu, W. R., & Long, A. C. (2011). Rate dependent modelling of the forming behaviour of viscous textile composites. *Composites Part A: Applied Science and Manufacturing*, 42(11), 1719-1726.

[18] Haanappel, S. P., ten Thije, R. H. W., Sachs, U., Rietman, B., & Akkerman, R. (2014). Formability analyses of uni-directional and textile reinforced thermoplastics. *Composites Part A: Applied Science and Manufacturing*, 56, 80-92.

[19] R. Akkerman, S.P. Haanappel, (2015) Thermoplastic composites manufacturing by thermoforming, Advances in Composites, Manufacturing and Process Design, Woodhead Publishing, 111-128

[20] Kaliske, M. (2000). A formulation of elasticity and viscoelasticity for fibre reinforced material at small and finite strains. *Computer Methods in Applied Mechanics and Engineering*, 185(2), 225-243.

[21] Lessard, H., Lebrun, G., Benkaddour, A., & Pham, X. T. (2015). Influence of process parameters on the thermostamping of a [0/90] 12 carbon/polyether ether ketone laminate. *Composites Part A: Applied Science and Manufacturing*, 70, 59-68.

[22] Harrison, P., Gomes, R., & Curado-Correia, N. (2013). Press forming a 0/90 cross-ply advanced thermoplastic composite using the double-dome benchmark geometry. Composites Part A: Applied Science and Manufacturing, 54, 56-69.

[23] Yu, W. R., Pourboghrat, F., Chung, K., Zampaloni, M., & Kang, T. J. (2002). Non-orthogonal constitutive equation for woven fabric reinforced thermoplastic composites. Composites Part A: Applied Science and Manufacturing, 33(8), 1095-1105.

[24] Simo, J. C. (1987). On a fully three-dimensional finite-strain viscoelastic damage model: formulation and computational aspects. *Computer methods in applied mechanics and engineering*, 60(2), 153-173.

[25] Lebrun, G., Bureau, M. N., & Denault, J. (2003). Evaluation of bias-extension and picture-frame test methods for the measurement of intraply shear properties of PP/glass commingled fabrics. *Composite structures*, 61(4), 341-352.

[26] Harrison, P., Clifford, M. J., & Long, A. C. (2004). Shear characterisation of viscous woven textile composites: a comparison between picture frame and bias extension experiments. *Composites Science and Technology*, 64(10), 1453-1465.

[27] Wang, P., Hamila, N., Pineau, P., & Boisse, P. (2014). Thermomechanical analysis of thermoplastic composite prepregs using bias-extension test. *Journal of Thermoplastic Composite Materials*, 27(5):679–98, doi: 10.1177/0892705712454289

[28] Liang, B., Hamila, N., Peillon, M., & Boisse, P. (2014). Analysis of thermoplastic prepreg bending stiffness during manufacturing and of its influence on wrinkling simulations. *Composites Part A: Applied Science and Manufacturing*, 67, 111-122.

[29] Piorkowska, E., & Rutledge, G. C. (Eds.). (2013). Handbook of polymer crystallization. John Wiley & Sons.

[30] Özdemir, I., Brekelmans, W. A. M., & Geers, M. G. D. (2008). Computational homogenization for heat conduction in heterogeneous solids. *International journal for numerical methods in engineering*, 73(2), 185-204.

[31] Naouar, N., Vidal-Sallé, E., Schneider, J., Maire, E., & Boisse, P. (2014). Meso-scale FE analyses of textile composite reinforcement deformation based on X-ray computed tomography. *Composite Structures*, 116, 165-176.

[32] Pazmino, J., Carvelli, V., & Lomov, S. V. (2014). Micro-CT analysis of the internal deformed geometry of a non-crimp 3D orthogonal weave E-glass composite reinforcement. *Composites Part B: Engineering*, 65, 147-157.

[33] Long, A. C., & Brown, L. P. (2011). Modelling the geometry of textile reinforcements for composites: TexGen. Composite reinforcements for optimum performance. Cambridge: Woodhead Publishing Ltd, 239–264.

[34] Mark, J. E. (2007). Physical Properties of Polymers Handbook. Springer.

[35] Mallick, P. K. (1997). Composites engineering handbook. CRC Press.

[36] Hasselman, D. P. H., Donaldson, K. Y., & Thomas, J. R. (1993). Effective thermal conductivity of uniaxial composite with cylindrically orthotropic carbon fibers and interfacial thermal barrier. *Journal of composite materials*, 27(6), 637-644.

[37] Boisse, P., Hamila, N., Vidal-Sallé, E., & Dumont, F. (2011). Simulation of wrinkling during textile composite reinforcement forming. Influence of tensile, in-plane shear and bending stiffnesses. *Composites Science and Technology*, 71(5), 683-692.

[38] Holzapfel, G. A., & Gasser, T. C. (2001). A viscoelastic model for fiber-reinforced composites at finite strains: Continuum basis, computational aspects and applications. *Computer methods in applied mechanics and engineering*, 190(34), 4379-4403.

[39] Aimene, Y., Vidal-Sallé, E., Hagège, B., Sidoroff, F., & Boisse, P. (2009). A hyperelastic approach for composite reinforcement large deformation analysis. *Journal of Composite materials.*

[40] Charmetant, A., Orliac, J. G., Vidal-Sallé, E., & Boisse, P. (2012). Hyperelastic model for large deformation analyses of 3D interlock composite preforms. *Composites Science and Technology*, 72(12), 1352-1360.

[41] Wang, J., Page, J. R., & Paton, R. (1998). Experimental investigation of the draping properties of reinforcement fabrics. *Composites Science and Technology*, 58(2), 229-237.

[42] Cao, J., Akkerman, R., Boisse, P., Chen, J., Cheng, H. S., De Graaf, E. F., ... & Zhu, B. (2008). Characterization of mechanical behavior of woven fabrics: experimental methods and benchmark results. *Composites Part A: Applied Science and Manufacturing*, 39(6), 1037-1053.

[43] Syerko, E., Comas-Cardona, S., & Binetruy, C. (2015). Models for shear properties/behavior of dry fibrous materials at various scales: a review. *International Journal of Material Forming*, 8(1), 1-23, DOI 10.1007/s12289-013-1138-7

[44] P. Boisse, N. Hamila, A. Madeo, G. Hivet, F. dell'Isola. The bias-extension test for the analysis of in-plane shear properties of textile composite reinforcements and prepregs: A review, *International Journal of Material Forming*, submitted.

[45] Peng, X. Q., Cao, J., Chen, J., Xue, P., Lussier, D. S., & Liu, L. (2004). Experimental and numerical analysis on normalization of picture frame tests for composite materials. *Composites Science and Technology*, 64(1), 11-21.

[46] Dangora, L. M., Hansen, C. J., Mitchell, C. J., Sherwood, J. A., & Parker, J. C. (2015). Challenges associated with shear characterization of a cross-ply thermoplastic lamina using picture frame tests. *Composites Part A: Applied Science and Manufacturing*, 78, 181-190.

[47] De Bilbao, E., Soulat, D., Hivet, G., & Gasser, A. (2010). Experimental study of bending behaviour of reinforcements. *Experimental Mechanics*, 50(3), 333-351.

[48] Syerko, E., Comas-Cardona, S., & Binetruy, C. (2012). Models of mechanical properties/behavior of dry fibrous materials at various scales in bending and tension: A review. *Composites Part A: Applied Science and Manufacturing*, 43(8), 1365-1388.

[49] Dangora, L. M., Mitchell, C. J., & Sherwood, J. A. (2015). Predictive model for the detection of out-of-plane defects formed during textile-composite manufacture. *Composites Part A: Applied Science and Manufacturing*, 78, 102-112.

[50] Margossian, A., Bel, S., & Hinterhoelzl, R. (2015). Bending characterisation of a molten unidirectional carbon fibre reinforced thermoplastic composite using a Dynamic Mechanical Analysis system. *Composites Part A: Applied Science and Manufacturing*, 77, 154-163.

[51] Willems, A., Lomov, S. V., Verpoest, I., & Vandepitte, D. (2008). Optical strain fields in shear and tensile testing of textile reinforcements. *Composites Science and Technology*, 68(3), 807-819.

[52] Carvelli, V. (2011). Biaxial tensile properties of reinforcements in composites. *Composite reinforcements for optimum performance*, Woodhead Publishing, 306-329

[53] Software ''PlasFib''. Inter Deposit certification, agence pour la protection des programmes. Paris, 2011

[54] Onate, E., & Cervera, M. (1993). Derivation of thin plate bending elements with one degree of freedom per node: a simple three node triangle. *Engineering computations*, 10(6), 543-561.

[55] Sabourin, F., & Brunet, M. (1995). Analysis of plates and shells with a simplified three-node triangular element. *Thin-walled structures*, 21(3), 209-223.

[56] Hamila, N., Boisse, P., Sabourin, F., & Brunet, M. (2009). A semi-discrete shell finite element for textile composite reinforcement forming simulation. *International journal for numerical methods in engineering*, 79(12), 1443-1466.

[57] Savija, I., Culham, J. R., Yovanovich, M. M., & Marotta, E. E. (2003). Review of thermal conductance models for joints incorporating enhancement materials. *Journal of Thermophysics and Heat transfer*, 17(1), 43-52.

[58] Skordos, A. A., Aceves, C. M., & Sutcliffe, M. P. (2007). A simplified rate dependent model of forming and wrinkling of pre-impregnated woven composites. *Composites Part A: Applied science and manufacturing*, 38(5), 1318-1330.

[59] Gutowski, T. G., Cai, Z., Bauer, S., Boucher, D., Kingery, J., & Wineman, S. (1987). Consolidation experiments for laminate composites. *Journal of Composite Materials*, 21(7), 650-669.

[60] Lee, W. I., & Springer, G. S. (1987). A model of the manufacturing process of thermoplastic matrix composites. *Journal of composite materials*, 21(11), 1017-1055.

[61] Dirk, H. J. L., Potter, K. D., & Eales, J. (2013). A concept for the in situ consolidation of thermoset matrix prepreg during automated lay-up. *Composites Part B: Engineering*, 45(1), 538-543.

[62] Hauptmann, R., & Schweizerhof, K. (1998). A systematic development of 'solid-shell' element formulations for linear and non-linear analyses employing only displacement degrees of freedom. *International Journal for Numerical Methods in Engineering*, 42(1), 49-69.

[63] Soulat, D., Cheruet, A., & Boisse, P. (2006). Simulation of continuous fibre reinforced thermoplastic forming using a shell finite element with transverse stress. *Computers & structures*, 84(13), 888-903.

[64] Kelly, P. A., Umer, R., & Bickerton, S. (2006). Viscoelastic response of dry and wet fibrous materials during infusion processes. *Composites Part A: Applied Science and Manufacturing*, 37(6), 868-873.

[65] Kelly, P. A. (2011). Transverse compression properties of composite reinforcements. *Composite reinforcements for optimum performance*, Woodhead Publishing, 333-366.

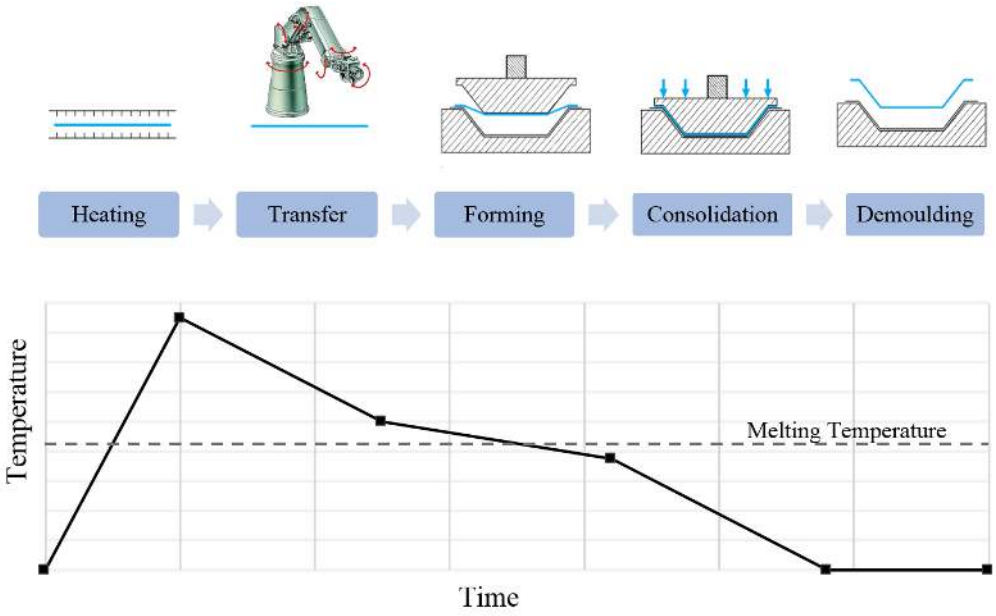

Fig. 1. Stages of the thermoforming process.

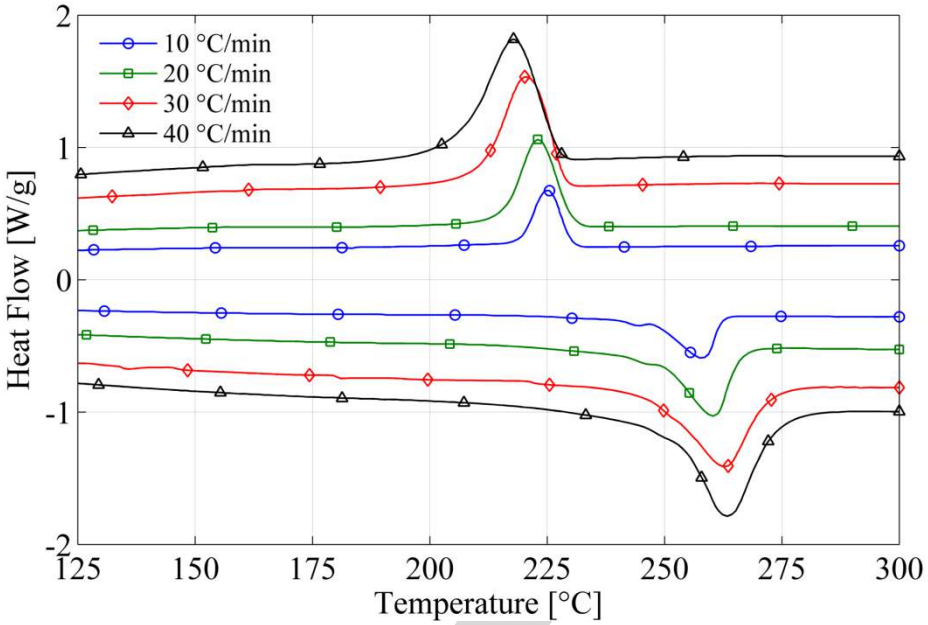

Fig. 2. DSC analysis for different temperature rates

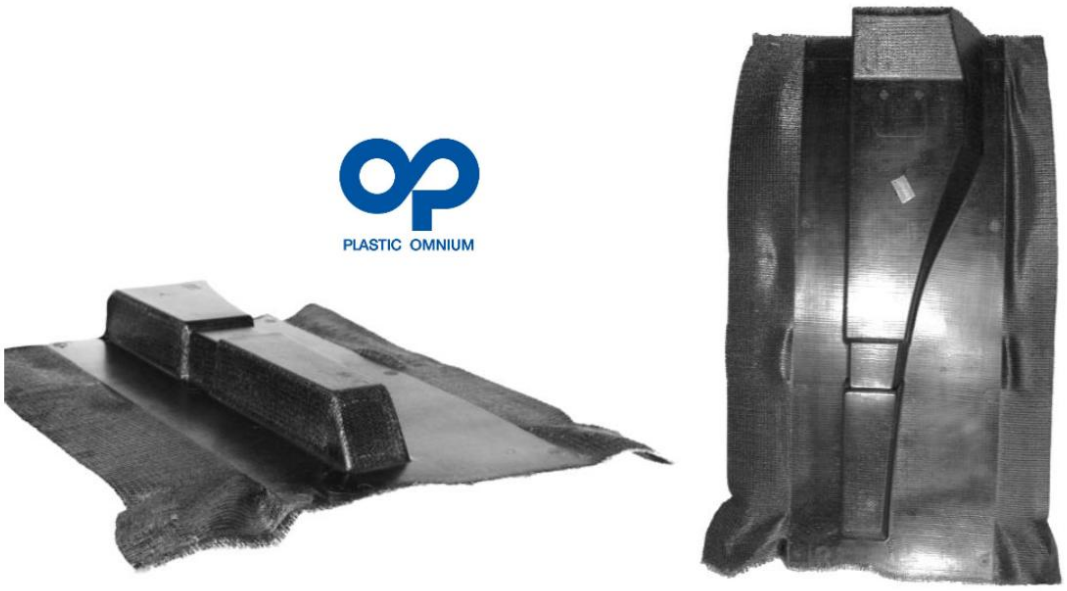

Fig 3. The manufactured composites part

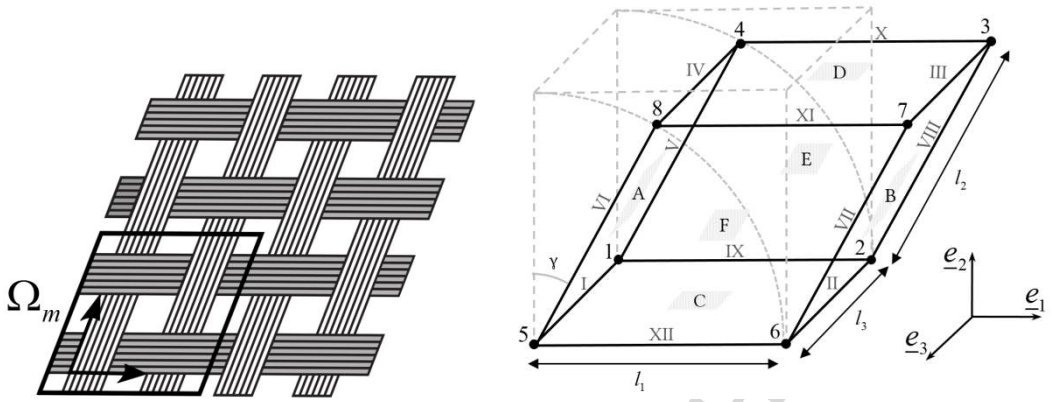

(a) (b)

Fig. 4. RVE of a woven fabric (a). Parametrization of the boundary of the RVE (b)

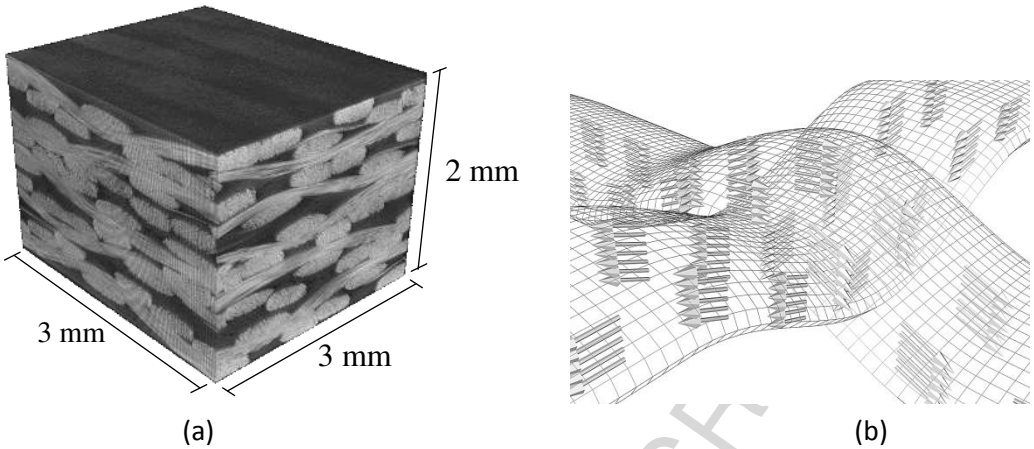

Fig. 5. Micro-CT image of the prepreg (a), orientation of the fibres (b)

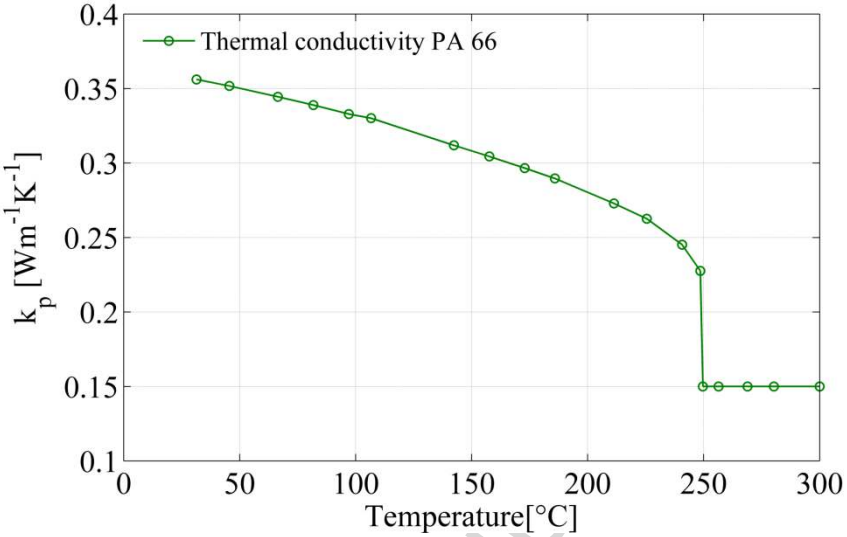

Fig. 6. Thermal conductivity PA 6.6 versus temperature

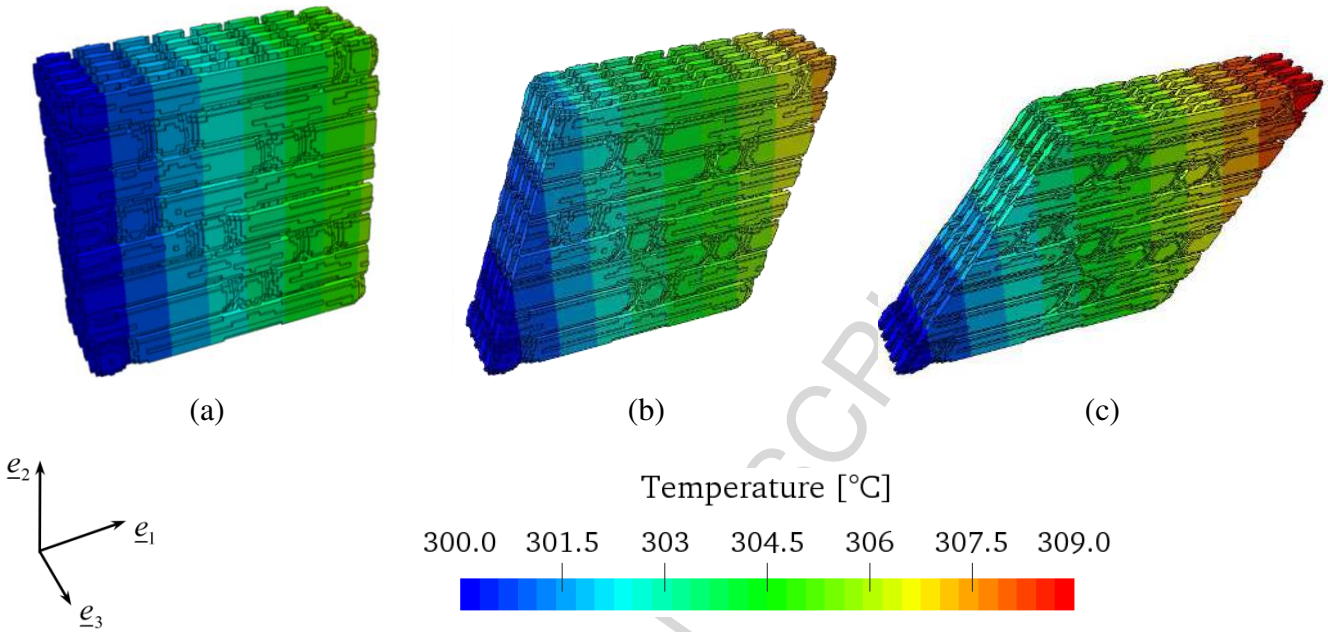

Fig. 7. Macroscopic temperature gradient in the direction 1
at T=300°C for different shear angles (a) 0°, (b) 20° and (c) 40°.

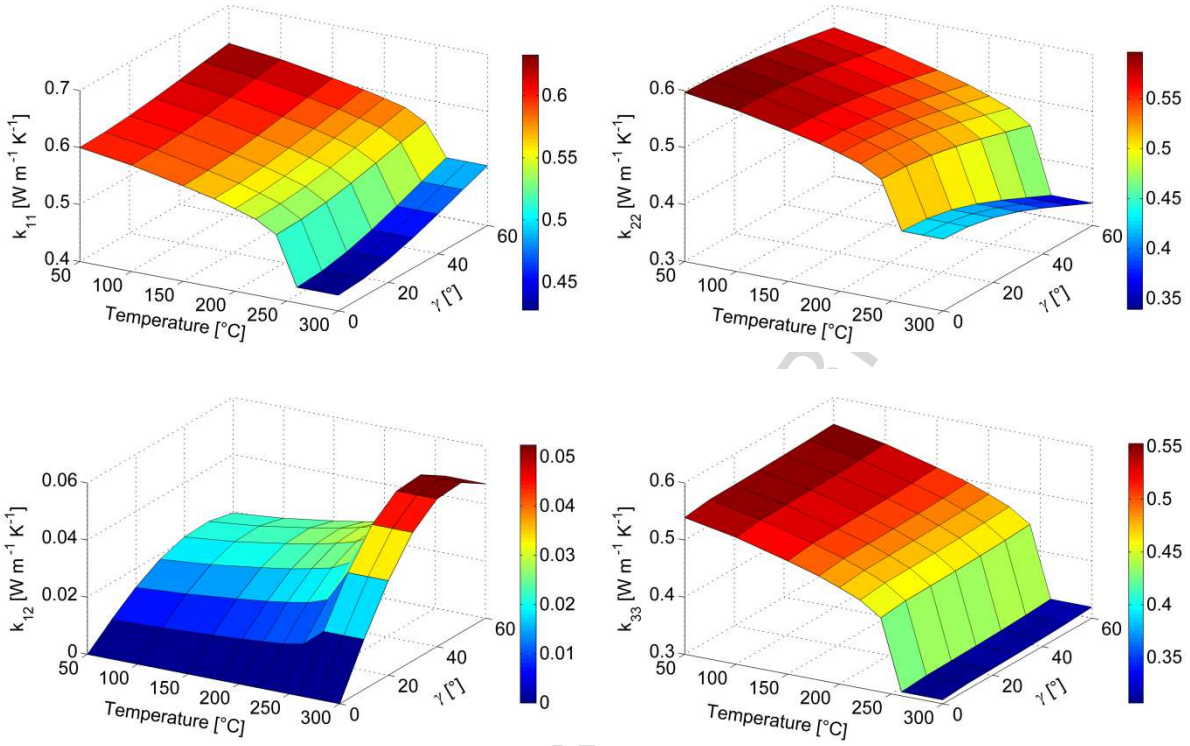

Fig. 8. Computed conductivity components as a function of temperature and shear angle.

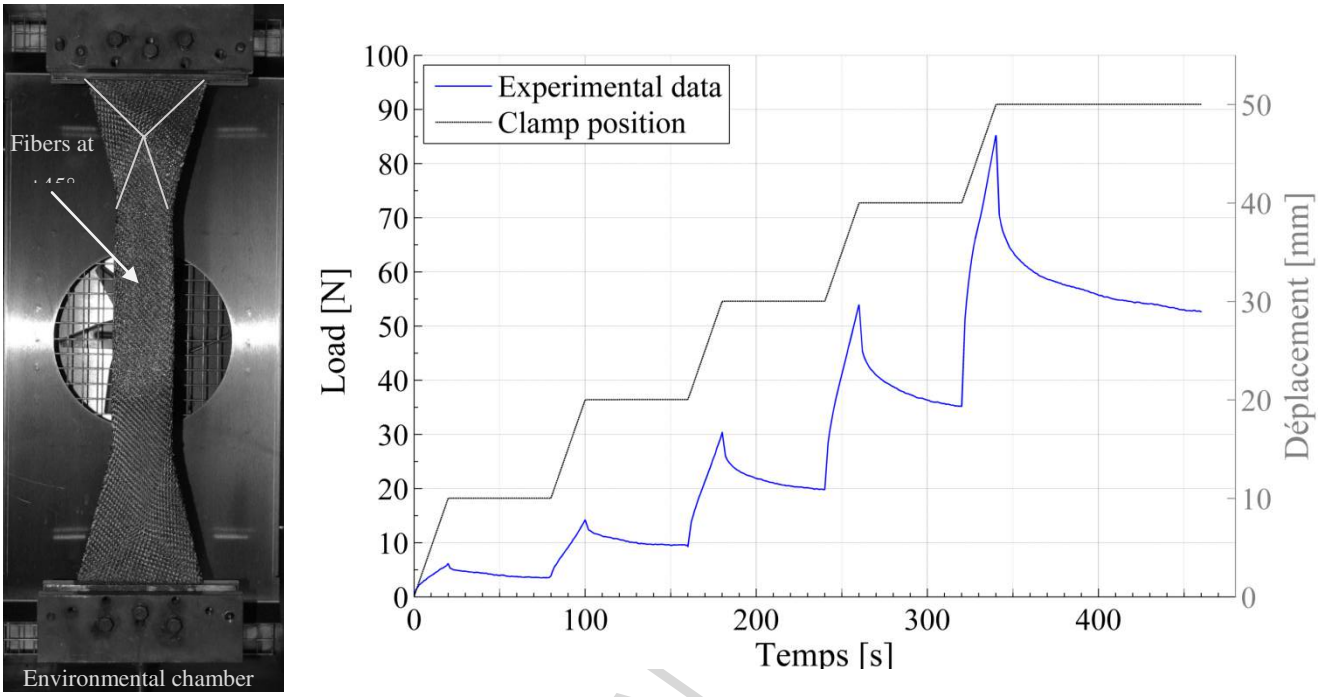

(a) (b)

Fig. 9. Bias extension test performed at 270°C. (a) Experimental (b) Load versus time curve increasing the displacement of the clamp per stage.

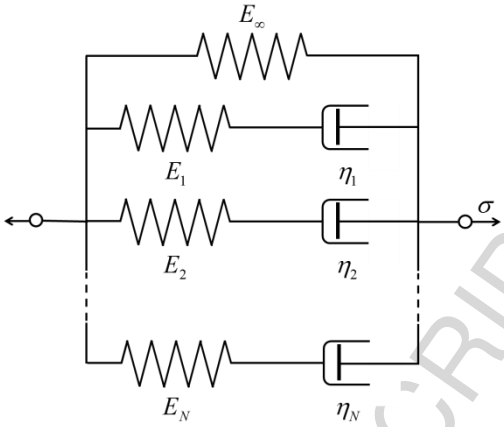

Fig. 10. Generalized 1D relaxation model

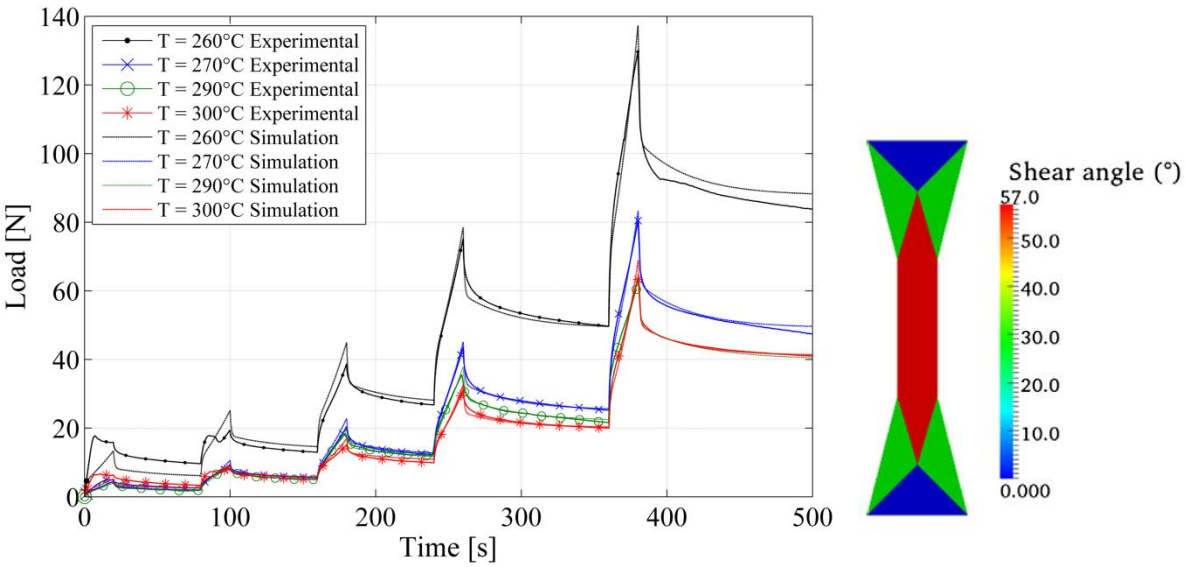

Fig. 11. Identification of the in-plane shear properties at different temperatures from bias extension tests.

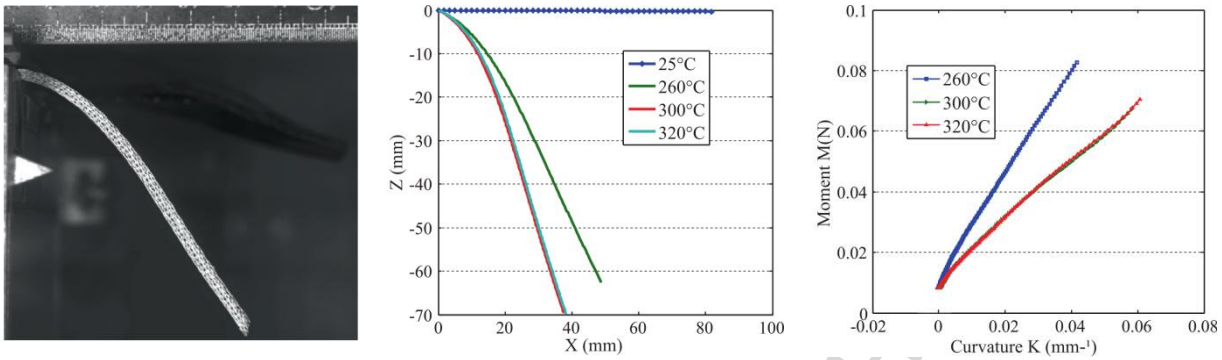

(a) (b) (c)

Fig. 12. Cantilever bending test at different temperatures [28]. (a) Experiment. (b) Measure of the deflection. (c) Curvature of the specimen

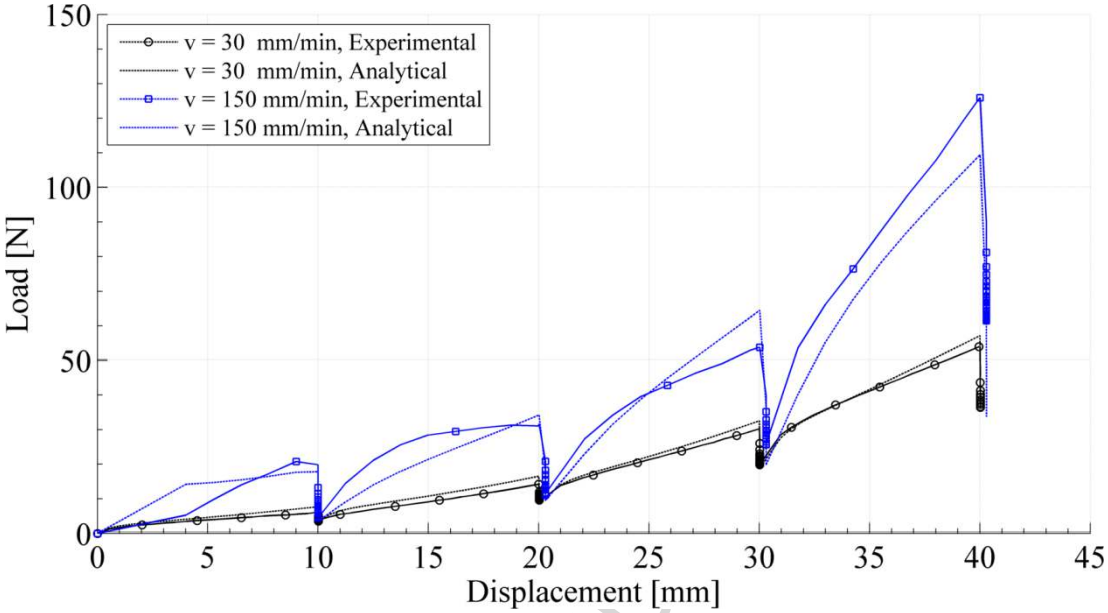

Fig. 13. Influence of the loading rate on the load

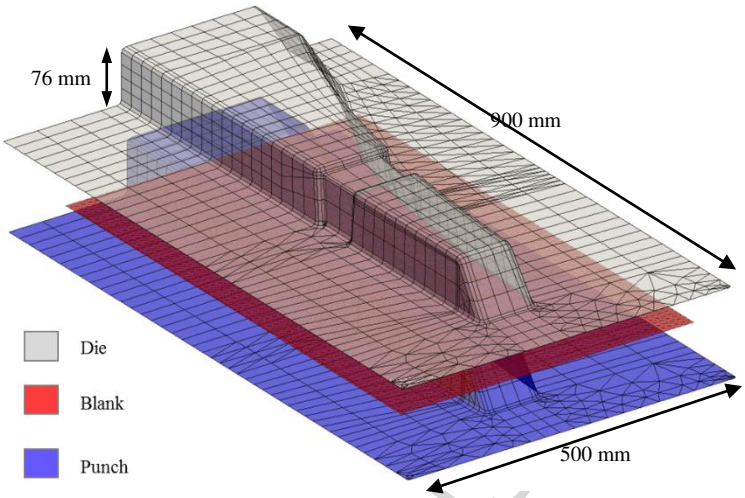

Fig. 14. Finite element mesh of the tools and of the blank.

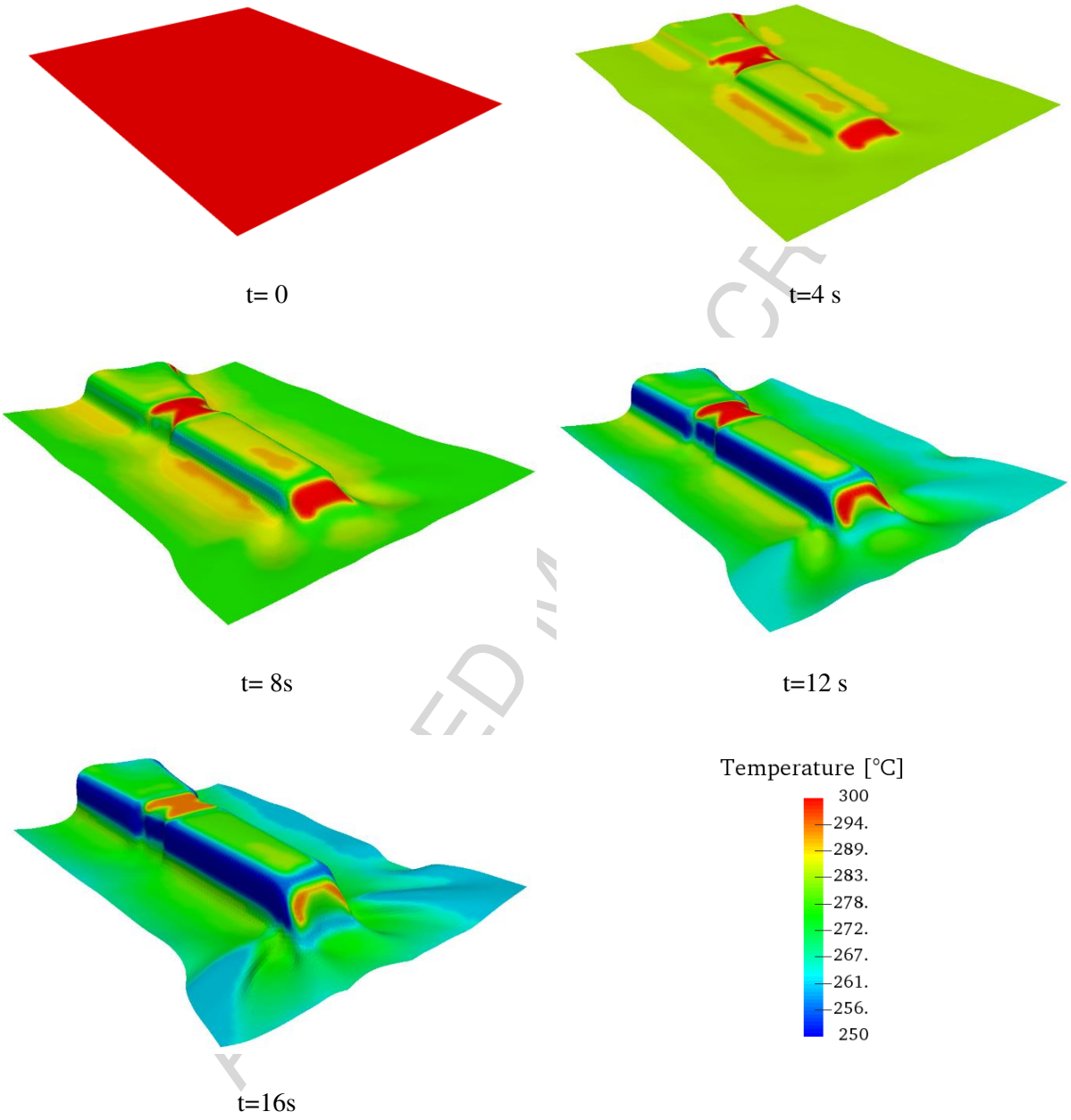

Fig. 15. In-plane temperature distribution during forming.

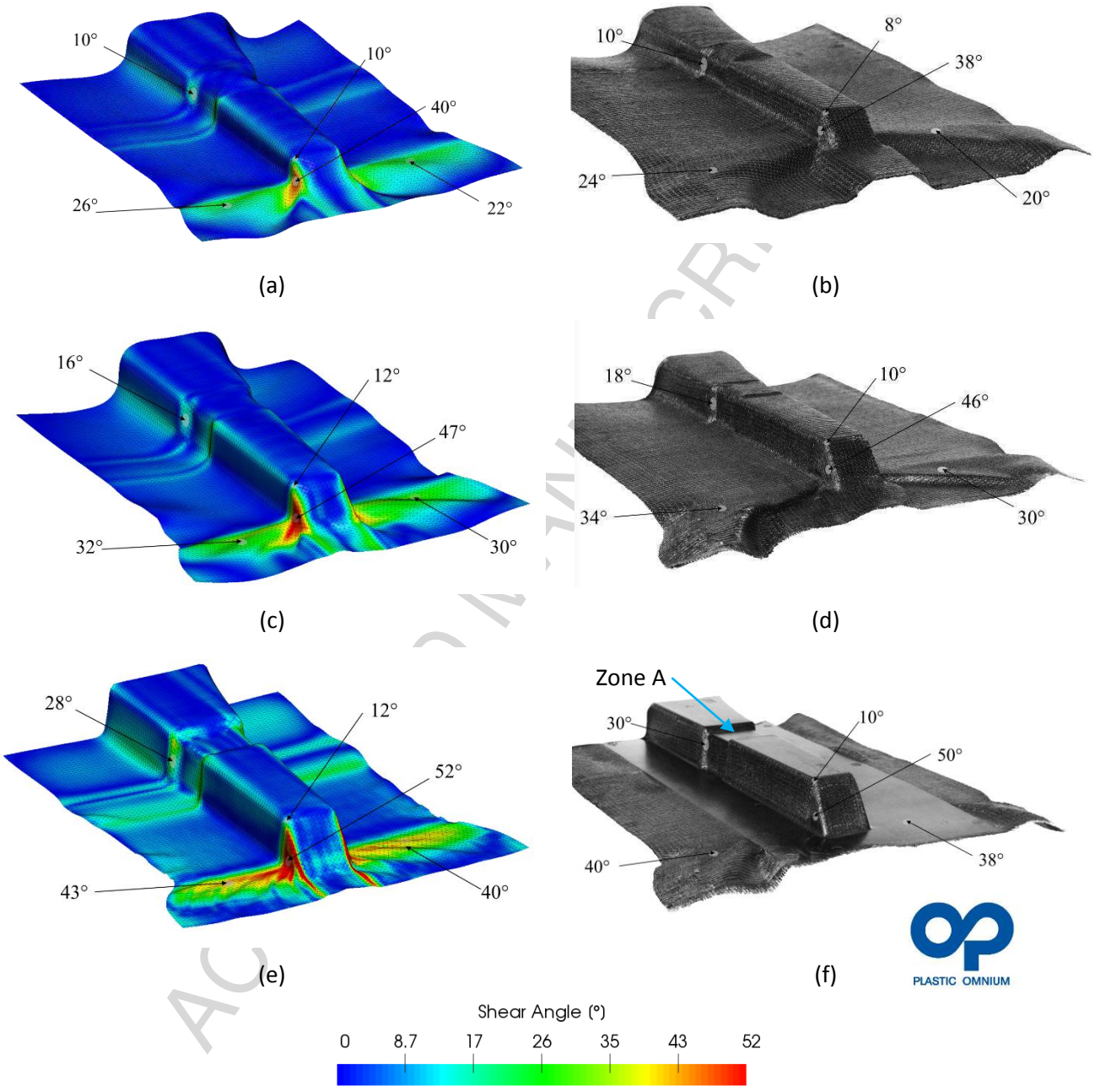

Fig. 16. Comparison between the experimental and numerical shape for (a), (b) 46 mm, (c), (d) 66 mm and (e), (f) 76 mm punch displacements.

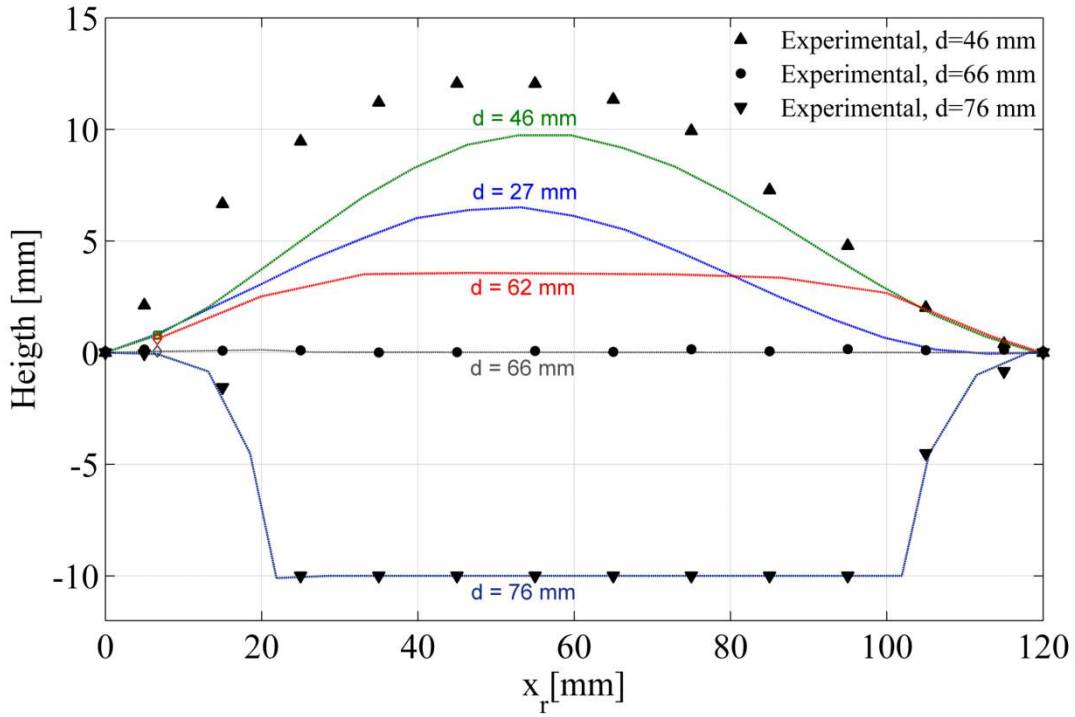

Fig. 17. Evolution of the geometrical bumps profile in zone A during forming and comparison with the experimental results.

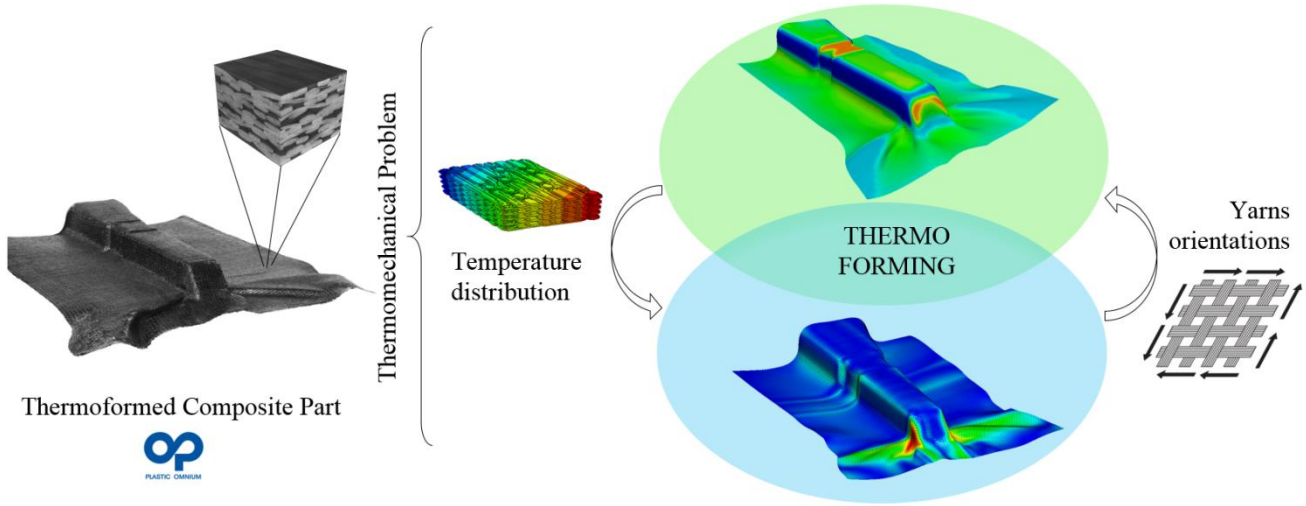

Graphical abstract

Highlights

Thermoplastic prepreg forming is simulated by alternate thermal and forming analyses.

The thermal conductivities are determined by mesoscopic analyses and homogenization

The viscous-hyperelastic model uses the convolution integrals

The thermoforming of an industrial part is realized both by experiments and simulation

The simulation of the thermoforming of an industrial part is compared to experiments